Journal of Applied Physics

RESEARCH ARTICLE | APRIL 01 2025

First principles studies of defect centers in two-dimensional NaCl associated with spin qubits

Special Collection: Defects in Solids for Quantum Technologies

Jijun Huang ; Qiang Ke ; Xueling Lei

J. Appl. Phys. 137, 134303 (2025)
https://doi.org/10.1063/5.0250329

Journal of Applied Physics ARTICLE pubs.aip.org/aip/jap

First principles studies of defect centers in two-dimensional NaCl associated with spin qubits

Cite as: J. Appl. Phys. **137**, 134303 (2025); doi: 10.1063/5.0250329
Submitted: 24 November 2024 · Accepted: 11 March 2025 ·
Published Online: 1 April 2025

Jijun Huang, Qiang Ke, and Xueling Lei[a)]

AFFILIATIONS

Department of Physics, Jiangxi Normal University, Nanchang, Jiangxi 330022, China

Note: This paper is part of the Special Topic, Defects in Solids for Quantum Technologies.
[a)]**Author to whom correspondence should be addressed:** xueling@jxnu.edu.cn

ABSTRACT

Spin defects in solids offer promising quantum bits (qubits) for quantum applications. However, the precise control of defect centers in three-dimensional (3D) crystals remains challenging. In contrast, two-dimensional (2D) materials provide a superior platform for both the controlled creation and precise manipulation of defect qubits. This work employs first-principles calculations to demonstrate that 2D NaCl exhibits high stability, a wide bandgap, and negligible spin–orbit coupling, making it a potential candidate for qubit host material. Among the eleven designed defects in 2D NaCl, the $Se_{Cl}V_{Na}$ defect exhibits advantages of spin triplet ground states, spin conservation in optical transitions, and the excited state energy of the dark state is higher than that of its triplet bright state. However, the critical qubit operation parameter, the zero-phonon line, remains relatively small. Notably, the zero-field splitting of the $Se_{Cl}V_{Na}$ defect falls within the microwave range, which is particularly suitable for quantum manipulation. Finally, the hyperfine tensors are calculated to assess the interaction between electron spin and nuclear spin. This study provides fundamental insights into the design principles of solid-state spin qubits in 2D materials for quantum technology application.

I. INTRODUCTION

In recent years, quantum technology, including quantum computation,[1] quantum communication,[2,3] and quantum sensing,[4,5] has attracted significant attention.[6,7] The core of this technology lies in the quantum bit (qubit), which has been a focal point of research. Various systems, including cold atomic systems,[8] superconductivity,[9,10] quantum dots,[11] and solid-state spin systems,[12–14] have been extensively explored for qubit implementation. In particular, solid-state spin systems have recognized diamond as a highly successful qubit host material, primarily due to its millisecond-scale spin coherence time of the negative charged nitrogen vacancy defect center (NV^-)[15,16] and the capability for initialization, manipulation, and readout at room temperature.[17] However, NV^-'s optical property is limited, with only ~4% of photons emitted from the zero-phonon lines (ZPLs).[18] In contrast, the negatively charged silicon vacancy defect center (SiV^-) in diamond exhibits higher emission efficiency, with 70% of the fluorescence originating from the ZPL,[19] making it a promising single-photon source.[20] Beyond diamond, other semiconductor materials such as silicon carbide (SiC),[13,21–23] boron nitride (BN),[24] zinc oxide (ZnO),[25] beryllium oxide (BeO),[26] magnesium oxide (MgO), calcium oxide (CaO),[27] and gallium nitride (GaN)[28] have been investigated as qubit host materials. Despite these efforts, the preparation of defect centers in three-dimensional (3D) host materials remains a significant challenge,[29] as both ion implantation and electron irradiation technologies can introduce lattice damage and unintended defects. These preparation-related side effects can lead to electric and magnetic field noise, thereby compromising spin coherence times and causing spectral diffusion of optical transitions.[30–32]

Recent research has explored two-dimensional (2D) qubit host materials as a promising solution. Researchers have achieved the precise positioning of defects within 2D materials using advanced techniques such as scanning tunneling microscopy (STM)[33] and focused ion beam (FIB).[34] For example, Cochrane *et al.* successfully fabricated carbon-doped defects (C_S) in WS_2 using STM in 2021.[33] Similarly, Glushkov *et al.* created various defect centers in hexagonal boron nitride (*h*-BN) employing FIB technology.[34] In addition to the ease of defect handling and manipulation, 2D materials also provide several other distinct advantages. For instance, the surface

defects in 2D materials exhibit a heightened sensitivity to the surrounding environment than the defects within 3D crystals, making them highly suitable for high-precision sensing applications. Moreover, the atomic-scale thickness of 2D materials facilitates their integration into smaller solid-state devices.[35,36] It has been reported that the 2D *h*-BN has been extensively studied as a host material of qubits due to its wide bandgap (~6 eV) and rich defect types.[37,38] Since Tran *et al.* first discovered the single-photon emission from *h*-BN in 2016,[39] numerous related works have been reported in succession.[40–48] Typically, the negatively charged boron vacancy defect center (V_B^-) has been observed to show an optically detected magnetic resonance (ODMR) response in the experiment.[49] Furthermore, the V_B^- defect center can be initialized and readout at room temperature[50] and can be widely applied in the magnetic field,[51] temperature,[52] and strain[53] sensing. However, the spin coherence time (T_2) of V_B^-[42] $(\sim 2.0\,\mu s)$ is one order of magnitude smaller than that of NV^- $(\sim 1.8$ ms), [15] which seriously hinders the application of V_B^- in quantum information. Therefore, in addition to some efforts to enhance the T_2 of V_B^-,[54,55] some new 2D materials such as WSe_2,[56] WS_2,[57] MoS_2,[58] and $MoSe_2$[29] have been proposed as qubit host materials.

In recent years, monolayer NaCl has attracted research interest. For example, Luo *et al.* predicted that 2D NaCl possesses a graphene-like structure with a bandgap of 6.302 eV, which is slightly larger than that of diamond (5.47 eV[59]) and *h*-BN (5.955 eV[37]), and exhibits excellent thermodynamic, kinetic, and mechanical stability.[60] Similarly, Thi *et al.* confirmed the kinetic and thermodynamic stability of 2D NaCl through phonon spectrum analysis and *ab initio* molecular dynamics (AIMD) simulations.[61] Furthermore, combining theoretical simulations with experimental methods, Tikhomirova *et al.* found a monolayer *h*-NaCl on the diamond (110) surface.[62] As a new 2D monolayer material, how about it serving as a host material for qubit? In this work, for the first time, we systematically studied various defects in 2D NaCl crystals using first-principles calculations to evaluate the potential of 2D NaCl as a qubit host material. This work not only presents a new potential 2D qubit host material but also contributes to the development of a qubit platform in 2D solid-state spin systems.

II. COMPUTATIONAL DETAILS

The first-principles calculations were performed using the Vienna *Ab initio* Simulation Package (VASP)[63,64] based on density functional theory (DFT). The projector augmented wave method (PAW) was employed to describe ion–electron interactions,[65,66] with a cutoff energy of 320 eV for the primitive cell and 520 eV for the supercell with various spin defects. The exchange-correlation energy was described by the Perdew–Burke–Ernzerhof functional under generalized gradient approximation (GGA-PBE).[67] To avoid interactions between periodically repeating images, a vacuum region of 20 Å was established along the z-direction. A $9 \times 9 \times 1$ supercell containing 162 atoms was used to construct defect models. The convergence criteria for structural optimization were set to 0.01 eV/Å for Hellmann–Feynman forces and 10^{-5} eV for total energies in the primitive cell, 0.02 eV/Å and 10^{-4} eV for the supercell, respectively. The Monkhorst–Pack scheme[68] was used to sample the k-points in the first Brillouin zone, whereas $6 \times 6 \times 1$ and $1 \times 1 \times 1$ k-meshes were employed for the primitive cell and the supercell, respectively. For projected density of states (PDOS) calculations, gaussian smearing (ISMEAR = 0) with a small SIGMA = 0.05 was applied, using $12 \times 12 \times 1$ and $1 \times 1 \times 1$ k-meshes for the primitive cell and the supercell, respectively. The Heyd–Scuseria–Ernzerhof (HSE06) hybrid functional[69,70] with a mixed parameter of 0.25 for the Hartree–Fock exchange term was utilized in the electronic structure calculations of the primitive cells and supercells with $S_{Cl}V_{Na}$, $Se_{Cl}V_{Na}$, and $Te_{Cl}V_{Na}$ defect centers. Thermal stability was evaluated through AIMD simulations in the NVT ensemble, using a $6 \times 6 \times 1$ supercell and a $1 \times 1 \times 1$ k-mesh, running for 10 ps with a time step of 2 fs at 300 K. To evaluate the dynamical stability, phonon dispersion calculations were conducted using the PHONOPY code[71] and the finite displacement method, where a $8 \times 8 \times 1$ supercell with a cutoff energy of 400 eV was employed. The ΔSCF method was used to calculate electronic excited states.[72]

III. RESULTS AND DISCUSSION

A. Structure and stability of 2D NaCl

Monolayer NaCl has a graphene-like structure with a space group of P$\bar{6}$m2 (No.187), as shown in Fig. 1(a). Each Na atom is coordinated by three Cl atoms, and conversely, each Cl atom is surrounded by three Na atoms. Our results yield a Na–Cl bond length of 2.620 Å and a lattice constant of 4.539 Å, which are in agreement with the previously reported values of 2.619 and 4.536 Å, respectively.[60] Figure 1(b) reveals that NaCl is a wide bandgap semiconductor with an indirect bandgap of 6.31 eV calculated at the HSE06 level, consistent with the recently reported theoretical value of 6.32 eV.[61] Furthermore, it is observed that the energy bands calculated at the PBE level, both with and without spin–orbital coupling (SOC), are almost completely overlapped, indicating that SOC has a small impact on the electronic structure of 2D NaCl. This characteristic satisfies the requirements for NaCl as a qubit host material.[73]

The cohesive energy of materials is a critical indicator of their stability and the feasibility of experimental synthesis. For 2D NaCl, the cohesive energy is defined as

$$E_{coh} = \frac{E_{NaCl} - E_{Na} - E_{Cl}}{2}, \quad (1)$$

where E_{NaCl} is the total energy of the 2D NaCl structure, and E_{Na} and E_{Cl} are the energies of isolated Na and Cl atoms, respectively. The calculated cohesive energy for 2D NaCl is −2.95 eV/atom, which is comparable to the theoretical values of 2D $MnSe_2$ (−2.86 eV/atom)[74] and VSi_2As_4 (−2.81 eV/atom),[75] suggesting that the 2D monolayer NaCl structure is energetically stable. Furthermore, we employed AIMD simulations to evaluate the thermodynamic stability of 2D NaCl. As shown in Fig. 1(c), the Na–Cl bonds remain intact during the heating process at 300 K for10 ps simulations, which is consistent with the results of Ref. 60. In addition, the phonon dispersions of 2D NaCl were calculated to confirm its dynamic stability, as shown in Fig. 1(d). The absence of imaginary frequencies throughout the Brillouin zone confirms the

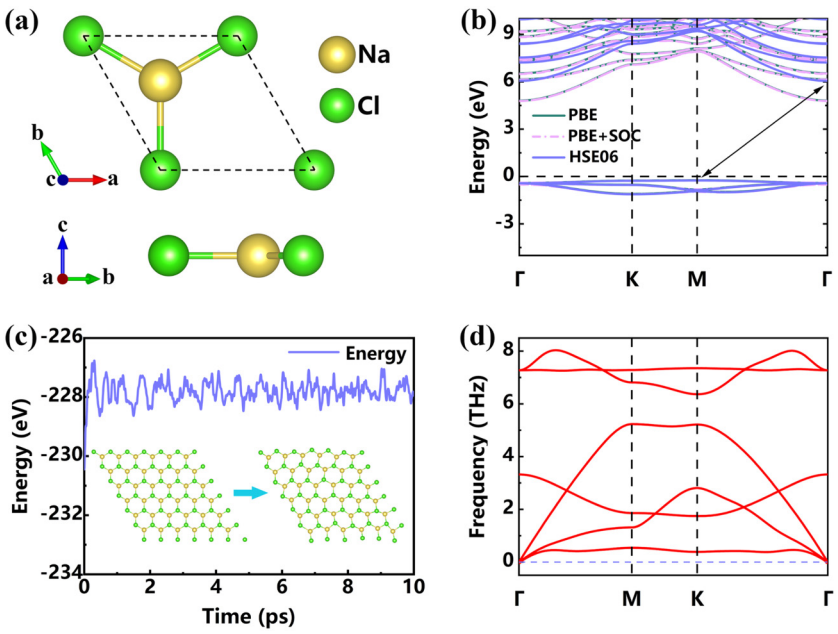

FIG. 1. (a) Top view and side view of the 2D NaCl structure; (b) energy band structure calculated at the PBE, PBE + SOC, and HSE06 levels; (c) AIMD results; and (d) the phonon spectrum.

dynamic stability of 2D NaCl. This also indicates that 2D NaCl can be experimentally prepared due to its thermal and dynamic stability.

B. Spin defects in 2D NaCl

In this work, we employ the following criteria to identify spin defects in 2D NaCl that are suitable for qubit applications:[29,73] first, the presence of a spin triplet ground state, akin to the NV^- center in diamond; second, spin conservation in optical transition for spin state readout; and third, defect energy levels positioned within the bandgap, separated from both the conduction band minimum (CBM) and valence band maximum (VBM) of the host material by at least 0.5 eV.[76] Three types of spin defects in 2D NaCl have been designed and optimized: vacancy defects, including Na vacancy (V_{Na}), Cl vacancy (V_{Cl}), and Na and Cl double vacancy ($V_{Na}V_{Cl}$); doping defects, such as the substitution of a Cl atom by O (O_{Cl}), S (S_{Cl}), Se (Se_{Cl}), and Te (Te_{Cl}); and vacancy-doping defect pairs, including $O_{Cl}V_{Na}$, $S_{Cl}V_{Na}$, $Se_{Cl}V_{Na}$, and $Te_{Cl}V_{Na}$. The configurations of all spin defects are shown in Fig. 2(a).

Figures 2(b)–2(d) show the average PDOS in a 2D NaCl structure with various types of spin defects. It is clear that the defect states associated with V_{Cl} and V_{Na} single vacancy exhibit spin polarization, whereas the defect states of $V_{Na}V_{Cl}$ double vacancy are non-spin-polarized. For V_{Cl}, the Fermi level is situated between the spin up and spin down defect states, indicating that it does not comply with the spin conservation condition in optical transitions. For the case of V_{Na}, the defect state is very close to the VBM of the host material, which does not satisfy the third criterion to identify spin defects. Conversely, for the defects O_{Cl}, S_{Cl}, Se_{Cl}, and Te_{Cl}, all exhibit spin-polarized defect states where the Fermi level is positioned between two spin-down defect states, ensuring spin conservation in optical transitions and thus satisfying the second identified criterion for potential qubits. Table S1 in the supplementary material summarizes the total magnetic moment and partial orbital occupation of these defects, indicating that these defect states are spin double ground states due to the single spin-up electron occupation ($S = 1/2$), and thus do not meet the first screening criterion. To achieve a spin triplet state, we changed the charge states by adding or removing electrons and analyzed their electronic structures. As shown in Fig. S1 in the supplementary material, surprisingly, the spin-polarized defect states vanished for the negatively charged O_{Cl}^-, S_{Cl}^-, Se_{Cl}^-, and Te_{Cl}^-, replaced by non-spin-polarized singlet states. This can be explained by the fact that the added electron occupies the empty spin-down defect state of neutral O_{Cl}, S_{Cl}, Se_{Cl}, and Te_{Cl}, pairing with the single spin-up electron, leading to fully occupied paired electrons and the disappearance of spin-polarized defect states. On the other hand, the defect states of the positively charged O_{Cl}^+, S_{Cl}^+, Se_{Cl}^+, and Te_{Cl}^+ are very close to the VBM of the host material, which does not meet the third criterion to identify spin defects. Consequently, both vacancy defects and doping defects are no longer considered viable qubit platforms.

Next, we explore the electronic structures of vacancy-doping defect pairs in 2D NaCl. As illustrated in Fig. 2(d), similar to the single vacancy V_{Na} and positively charged O_{Cl}^+, S_{Cl}^+, Se_{Cl}^+, and Te_{Cl}^+, the defect state of $O_{Cl}V_{Na}$ is also very close to the VBM of the host material, and is not suitable for spin defects. In contrast, the defect states involved in electron transitions for the $S_{Cl}V_{Na}$, $Se_{Cl}V_{Na}$, and $Te_{Cl}V_{Na}$ defect pairs are well-separated from the host material's electronic states, and remain in the spin conservation state in optical transitions. It is evident from Table S1 in the supplementary material that the defect states of $S_{Cl}V_{Na}$, $Se_{Cl}V_{Na}$, and $Te_{Cl}V_{Na}$ are the spin triplet ground states, due to the

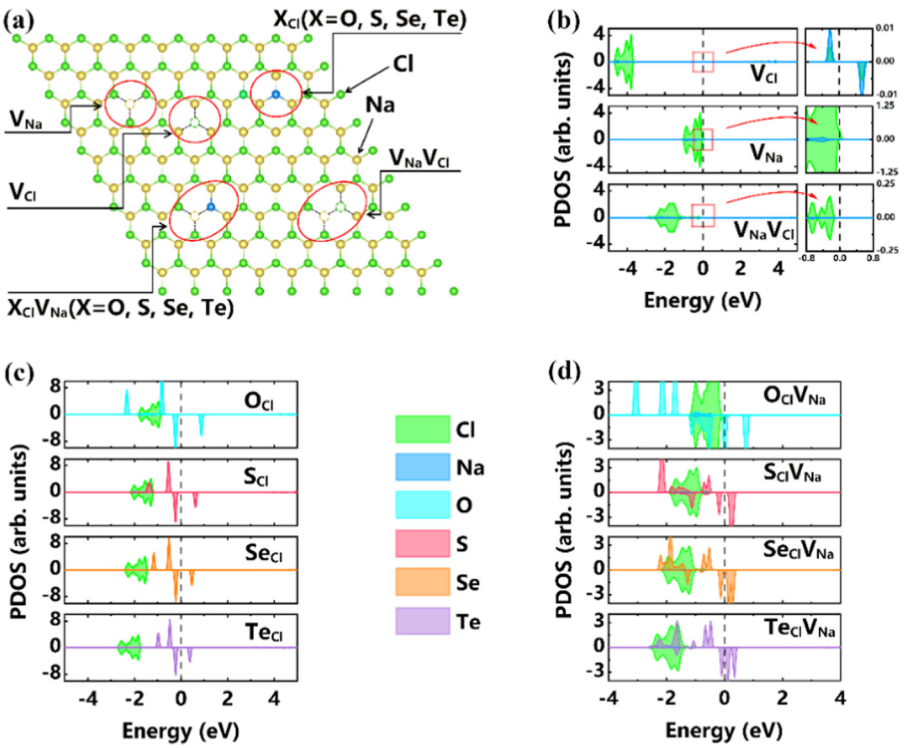

FIG. 2. Schematic diagram of various defects in 2D NaCl (a), the average projected density of states (PDOS) on each atom with various vacancy defects (b), doping defects (c), and vacancy-doping defect pairs (d) at the PBE level.

occupation of two spin-up electrons ($S = 1$). Furthermore, Table S2 in the supplementary material lists the energies of triplet and singlet ground states of these three defects along with the energy difference. It confirms again that the triplet states of these defects are ground states. These electronic structural features suggest that the $S_{Cl}V_{Na}$, $Se_{Cl}V_{Na}$, and $Te_{Cl}V_{Na}$ defect centers in 2D NaCl are potential candidates for qubit realization.

Moreover, it is noteworthy that O, S, Se, and Te all belong to the same main group and possess an equal number of valence electrons. Despite this similarity, the defect state of $O_{Cl}V_{Na}$ is unique among them. This can be attributed to the maximum electronegativity of the O atom compared to the other dopant atoms, resulting in the strongest interaction between the O atom and its neighboring Na atoms. To validate this hypothesis, the geometric structures of $O_{Cl}V_{Na}$, $S_{Cl}V_{Na}$, $Se_{Cl}V_{Na}$, and $Te_{Cl}V_{Na}$ have been examined, as depicted in Fig. S2 in the supplementary material. Our findings indicate that the bond lengths between the dopant atoms and their neighboring Na atoms follow the order d_{O-Na} (2.313 Å) < d_{S-Na} (2.898 Å) < d_{Se-Na} (3.039 Å) < d_{Te-Na} (3.250 Å), which is in line with the order of electronegativity of the dopant atoms. Consequently, the nearly linear Na–O–Na local structure contributes to the unique electronic properties of the $O_{Cl}V_{Na}$ defect.

To accurately determine the defect levels, the electronic structures of the $S_{Cl}V_{Na}$, $Se_{Cl}V_{Na}$, and $Te_{Cl}V_{Na}$ defect centers are calculated by the HSE06 hybrid functionals. The energy band structures are depicted in Fig. S3 in the supplementary material. The defect levels are schematically illustrated in Figs. 3(a), 3(c), and 3(e), while their corresponding wave functions are shown in Figs. 3(b), 3(d), and 3(f), respectively. It is to be noted that only the defect levels within the gap are illustrated, including the four highest occupied spin-up defect levels, the two highest occupied spin-down defect levels, and the two lowest unoccupied spin-down defect levels. All three defect centers, $S_{Cl}V_{Na}$, $Se_{Cl}V_{Na}$, and $Te_{Cl}V_{Na}$, belong to the C_{2v} symmetry group. Employing the C_{2v} point group symmetry, we identify the irreducible representations of the defect levels. To differentiate defect levels sharing the same irreducible representation, suffixes like $b_1(1)$ and $b_1(2)$ were appended. As previously discussed, spin-conserved optical transitions are essential at defect centers. Upon examining the defect levels of $S_{Cl}V_{Na}$, $Se_{Cl}V_{Na}$, and $Te_{Cl}V_{Na}$, there are two electronic transition pathways, $b_1(2) \rightarrow a_1$ and $b_1(2) \rightarrow b_2(2)$, both occurring within the spin-down defect levels. The transition dipole moments (TDM) for these pathways are calculated and the results are summarized in Table S3 in the supplementary material. It is evident that the TDM for the transition pathway $b_1(2) \rightarrow a_1$ is much larger than that for the transition pathway $b_1(2) \rightarrow b_2(2)$, suggesting that the $b_1(2) \rightarrow a_1$ transition is the most likely electronic transition, noted as red arrows in Figs. 3(a), 3(c), and 3(e), while the $b_1(2) \rightarrow b_2(2)$ transition is forbidden. The wave functions further support these findings. For the $S_{Cl}V_{Na}$, $Se_{Cl}V_{Na}$, and $Te_{Cl}V_{Na}$ defects, the wave functions corresponding to the $b_1(2)$ and a_1 orbitals are primarily confined to the plane, thereby promoting significant spatial overlap and facilitating electronic transitions. Conversely, the $b_2(2)$ wave function is predominantly located outside the plane, resulting in a minimal overlap with the $b_1(2)$ wave function and rendering electronic transitions less probable.

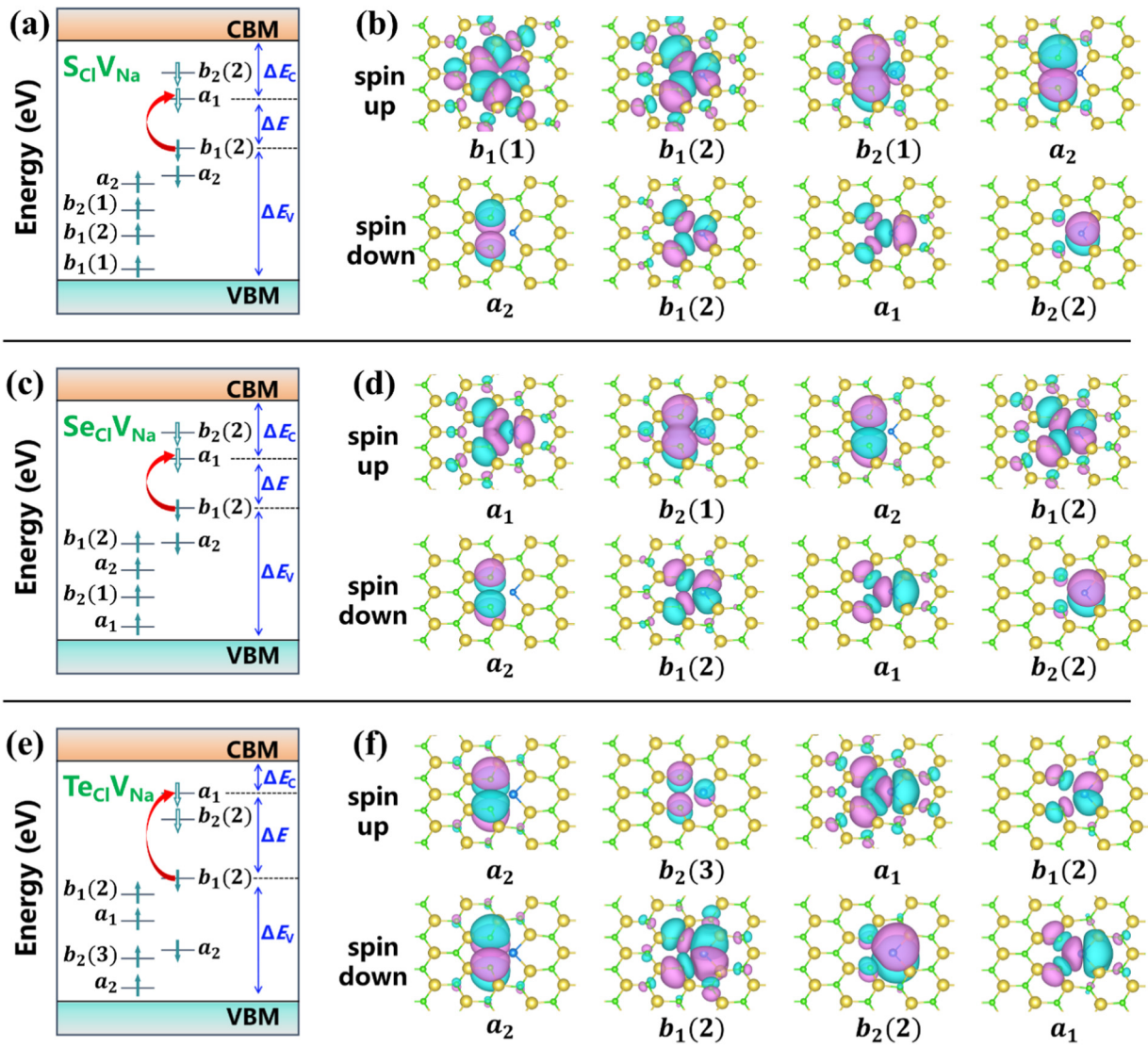

FIG. 3. Schematic diagram for defect levels of (a) $S_{Cl}V_{Na}$, (c) $Se_{Cl}V_{Na}$, and (e) $Te_{Cl}V_{Na}$. Green arrows indicate spin orientation, with and without green shading, denoting the electron occupied and unoccupied states, respectively. Red arrows represent electronic transitions. Wave functions for the corresponding defect levels of (b) $S_{Cl}V_{Na}$, (d) $Se_{Cl}V_{Na}$, and (f) $Te_{Cl}V_{Na}$. The isosurface value is 5×10^{-10} e/Å^3.

In addition, the energy gaps between the defect levels and the CBM of the host material, denoted as ΔE_C, as well as the gaps between the defect levels and the VBM of the host material, denoted as ΔE_V, should ideally be at least 0.5 eV. Table I lists ΔE_C, ΔE_V, and ΔE for optical transitions calculated at the HSE06 level. It is clear that all ΔE_C values exceed 3.0 eV, and the minimum ΔE_V value of 0.75 eV surpassing the recommended threshold of 0.5 eV, indicating that the defect levels are effectively separated from both the VBM and CBM of the host material.[76] Consequently, we propose that the $S_{Cl}V_{Na}$, $Se_{Cl}V_{Na}$, and $Te_{Cl}V_{Na}$ defect centers in 2D NaCl can serve as qubit platforms, and thereby proceed with further investigation.

The formation energy of defects is a critical parameter that reflects the likelihood of their generation within the host material, which can be calculated using the following formulas:[77]

$$E_{\text{form}}\left[X_{Cl}V_{Na}^{q}\right] = E_{\text{tot}}\left[X_{Cl}V_{Na}^{q}\right] + E_{\text{corr}}\left[X_{Cl}V_{Na}^{q}\right] - E_{\text{tot}}[\text{perfect}] - \sum_i n_i u_i + q\left(\Delta\varepsilon_F + \varepsilon_{\text{VBM}}^{\text{perfect}} - \Delta V_{0/p}\right) \quad (2)$$

and

$$\Delta V_{0/p} = V_{0|\text{far}} - V_p, \quad (3)$$

TABLE I. The energy gaps (eV) of ΔE_C, ΔE_V, and ΔE calculated at the HSE06 level.

Defects	ΔE_C	ΔE_V	ΔE
$S_{Cl}V_{Na}$	3.78	0.75	1.53
$Se_{Cl}V_{Na}$	3.50	1.00	1.52
$Te_{Cl}V_{Na}$	3.05	1.54	1.45

where $E_{tot}\left[X_{Cl}V_{Na}^{q}\right]$ and $E_{corr}\left[X_{Cl}V_{Na}^{q}\right]$ are the total energy and finite-size electrostatic correction energy of 2D NaCl with $X_{Cl}V_{Na}$ (X = S, Se, and Te) defects in the charge state q and E_{tot}[perfect] is the total energy of the perfect 2D NaCl. The electrostatic correction energy is calculated using the Freysoldt–Neugebauer–van de Walle (FNV) scheme,[78] as implemented in the CoFFEE code.[79] n_i represents the number of atoms of species i removed (negative value) or added (positive value) from the supercell, and u_i represents the chemical potential of species i. Specifically, the chemical potentials of S, Se, and Te are derived from their respective stable elementary phase, and $\mu_{Na} + \mu_{Cl} = \mu_{NaCl}$, μ_{NaCl} is the total energy of a NaCl primitive cell. $\Delta\varepsilon_F$ stands for the Fermi level, which varies from 0 to the bandgap of 2D NaCl (6.31 eV). $\varepsilon_{VBM}^{perfect}$ refers to the VBM of the perfect 2D NaCl. $\Delta V_{0/p}$ represents a potential alignment term, which is obtained by comparing the electrostatic potentials from a pristine calculation (V_p) and far from the defect in a neutral defect calculation $(V_{0|far})$.[79]

The defect formation energies for $S_{Cl}V_{Na}$, $Se_{Cl}V_{Na}$, and $Te_{Cl}V_{Na}$ in the ±1, ±2, and 0 charge states have been calculated, as shown in Fig. 4(a), where the circles represent the positions of the charge transition levels. For the $S_{Cl}V_{Na}$ and $Se_{Cl}V_{Na}$ defects, it is evident that the charge transition levels for 0 and ±1 charge states are situated within the bandgap, whereas for ±2 charge states, they are located in VB and CB, respectively. Specifically, the charge transition levels $\varepsilon(+1|0)$ and $\varepsilon(0|-1)$ for the $S_{Cl}V_{Na}$ defect are 2.51 and 3.44 eV, respectively. Similarly, for the $Se_{Cl}V_{Na}$ defect, the charge transition levels $\varepsilon(+1|0)$ and $\varepsilon(0|-1)$ are 2.55 and 3.68 eV, respectively. In the case of the $Te_{Cl}V_{Na}$ defect, the charge transition levels for the +2, ±1, and 0 charge states are situated within the bandgap, only the −2 charge state is located in CB. Specifically, the charge transition levels $\varepsilon(+2|+1)$, $\varepsilon(+1|0)$, and $\varepsilon(0|-1)$ are 0.81, 1.76, and 4.05 eV, respectively. Clearly, in the range of the Fermi level of 0–6.31 eV, $S_{Cl}V_{Na}$ and $Se_{Cl}V_{Na}$ in the ±2 charge state and $Te_{Cl}V_{Na}$ in the −2 charge state are unstable. Furthermore, the defect formation energies of the neutral $S_{Cl}V_{Na}$ and $Se_{Cl}V_{Na}$ defects are 2.68 and 2.80 eV, respectively, both of which are lower than the 3.15 eV of the $Te_{Cl}V_{Na}$ defect. This suggests that the $S_{Cl}V_{Na}$ and $Se_{Cl}V_{Na}$ defects are more likely to be formed than the $Te_{Cl}V_{Na}$ defect. To assess the stability of vacancy-doping defect pairs, the binding energy of the defect pair was calculated by[80]

$$E_b(X_{Cl}V_{Na}) = E_{form}(X_{Cl}) + E_{form}(V_{Na}) - E_{form}(X_{Cl}V_{Na}), \quad (4)$$

where $E_{form}(V_{Na})$, $E_{form}(X_{Cl})$, and $E_{form}(X_{Cl}V_{Na})$ are the formation energies of V_{Na}, X_{Cl} (X = S, Se, Te), and the vacancy-doping defect pair $X_{Cl}V_{Na}$, respectively. A positive $E_b(X_{Cl}V_{Na})$ indicates that the defect pair is thermodynamically favorable. The binding energies are 1.22, 1.53, and 1.20 eV for the defect pairs $S_{Cl}V_{Na}$, $Se_{Cl}V_{Na}$, and $Te_{Cl}V_{Na}$, respectively, indicating that these defect pairs are thermodynamically stable. Furthermore, charge regulation alters the ground-state electron occupancy, thereby affecting the spin multiplicities of the defects. As illustrated in Fig. 4(b), the electron occupancy for the three defects is depicted across various charge states. It is evident that in both the neutral and −1 charge states, all three defects exhibit the same electron occupancy. The neutral charge states correspond to a spin triplet ($S = 1$), while the −1 charge states correspond to a spin doublet ($S = 1/2$). However, in the +1 charge states, the $S_{Cl}V_{Na}$ and $Se_{Cl}V_{Na}$ defects exhibit a spin doublet ($S = 1/2$), whereas the $Te_{Cl}V_{Na}$ defect shows a spin quadruplet ($S = 3/2$).

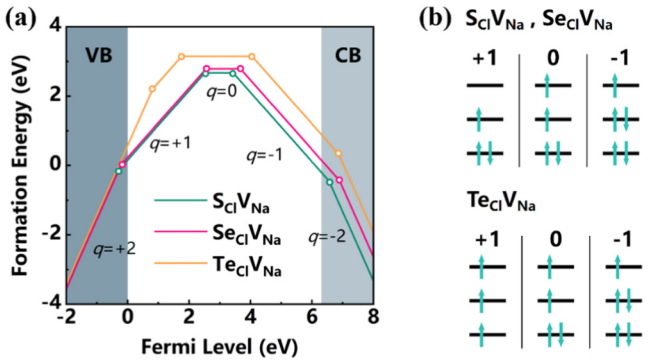

FIG. 4. (a) The defect formation energy of the $X_{Cl}V_{Na}$ (X = S, Se, Te) defect centers in different charge states, where the slope represents different charge states; (b) the ground-state electron occupancy in different charge states.

C. Zero-phonon lines, zero-field splitting, and hyperfine tensor

As aforementioned, the $b_1(2) \rightarrow b_2(2)$ optical transition is forbidden (dark state), while the $b_1(2) \rightarrow a_1$ optical transition is allowable (bright state). We know that if the dark state's level lies below that of the bright one, then no emission is likely because phonons can quickly cool the system to the lowest energy excited state. To evaluate whether the $S_{Cl}V_{Na}$, $Se_{Cl}V_{Na}$, and $Te_{Cl}V_{Na}$ defects can emit light, the excited state energies of these three defects for two transition pathways, $b_1(2) \rightarrow a_1$ and $b_1(2) \rightarrow b_2(2)$, have been calculated. As detailed in Table II, the excited state energy of the dark state for the $Se_{Cl}V_{Na}$ defect is higher than that of its triplet bright state. In contrast, the excited state energies of

TABLE II. The relative excited state energies (unit in eV) for the two transition pathways $b_1(2) \rightarrow a_1$ and $b_1(2) \rightarrow b_2(2)$ calculated at the HSE06 level.

Transition pathway	$S_{Cl}V_{Na}$	$Se_{Cl}V_{Na}$	$Te_{Cl}V_{Na}$
$b_1(2) \rightarrow a_1$	0.06	−0.05	0.03
$b_1(2) \rightarrow b_2(2)$	0.00	0.00	0.00

the dark states for the $S_{Cl}V_{Na}$ and $Te_{Cl}V_{Na}$ defects are lower than their respective triplet bright state. This indicates that only the $Se_{Cl}V_{Na}$ defect is possible to emit, while the $S_{Cl}V_{Na}$ and $Te_{Cl}V_{Na}$ defects are likely non-emissive. Therefore, we will only consider the $Se_{Cl}V_{Na}$ defect in the next study.

In the context of qubit operations, the ZPL plays a crucial role in both initialization and identification. Consequently, the operation parameter of the ZPL has been examined in the following. It is important to note that the absorption or emission of a photon not only changes the electronic wave function but also alters the atomic structure of defects, leading to distinct potential energy surfaces between the ground and excited states.[72] Consequently, it is essential to calculate the configuration coordinate of the defect centers. The schematic of the configuration coordinate is shown in Fig. 5, where the green and blue lines represent the vertical absorption and vertical emission transitions, respectively, and the orange line indicates the ZPL. The energy of the vertical absorption transition is determined by calculating the energy difference between the ground state and the excited state at the ground state structure. Similarly, the energy of the vertical emission transition is obtained by calculating the energy difference between the ground state and the excited state at the excited state structure. The energy difference between the lowest potential energy surfaces of the ground and excited states defines the ZPL, as listed in Table S4 in the supplementary material. It shows that the ZPL value for the $Se_{Cl}V_{Na}$ defect is only 0.21 eV, which is significantly lower than the 1.61 eV of C_BV_N[48] and the 1.60 eV of V_B^- in *h*-BN.[81]

Since the Huang–Rhys (HR) factor quantifies the number of phonons emitted during the transition, next, the HR factor has been evaluated. According to the one-dimensional configuration coordinate diagram (1D-CCD) method, the HR factor (S) is obtained as[36]

$$S = \frac{\lambda_g}{\hbar\Omega}, \tag{5}$$

where λ_g is the reorganization energy in the ground state and Ω is the effective vibrational frequency. Our calculated value of S is 10.40 for the $Se_{Cl}V_{Na}$ defect, indicating that there are many effective phonons that participated in the optical transition.

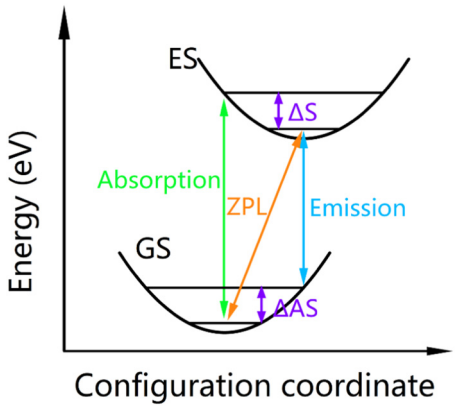

FIG. 5. The configuration coordinate diagram, where ΔS and ΔAS denote the Stokes and anti-Stokes shifts, respectively.

In addition, the Debye–Waller factor (*DW*) is calculated by the formula[82]

$$DW = e^{-S}. \tag{6}$$

According to the definition of *DW*, the larger the *S*, the smaller the *DW*. Our calculated value of *DW* is 3.03×10^{-5} for the $Se_{Cl}V_{Na}$ defect. Therefore, the Debye–Waller factor is rather small, indicating that non-radiative decay will be highly competitive with radiative decay during the transition.

Zero-field splitting (ZFS) is another crucial operation parameter in qubit manipulation, representing the energy splitting arising from the electron spin-spin dipole interaction between spin sublevels in the absence of an external magnetic field. It can be calculated using the following formula:[83]

$$\hat{H}_{ss} = -\frac{\mu_0}{4\pi}\frac{g^2\beta^2}{r^5}\left[3\left(\hat{\vec{s}}_1\cdot\vec{r}\right)\left(\hat{\vec{s}}_2\cdot\vec{r}\right) - \left(\hat{\vec{s}}_1\cdot\hat{\vec{s}}_2\right)\vec{r}^2\right], \tag{7}$$

where μ_0 is the magnetic permeability of vacuum, g is the electron's Landé factor, β is the Bohr magneton, $\hat{\vec{s}}_1$ and $\hat{\vec{s}}_2$ are the spin angular momentum operators of the two electrons, and $\vec{r}$ is the displacement vector between the two electrons. Furthermore, the total spin angular momentum operator, $\hat{\vec{S}} = \sum_i \hat{\vec{s}}_i$, can be introduced to separate the spatial and spin dependence, allowing formula (7) to be rewritten in a more explicit form

$$\begin{aligned}\hat{H}_{ss} &= \hat{\vec{S}}^{\mathrm{T}} D \hat{\vec{S}} = D_{xx}S_x^2 + D_{yy}S_y^2 + D_{zz}S_z^2 \\ &= D\left(S_z^2 - \frac{S(S+1)}{3}\right) + \frac{E\left(S_+^2 + S_-^2\right)}{2},\end{aligned} \tag{8}$$

where D is the ZFS tensor, which accounts for the energy splitting between the spin sublevels of the ground state and the excited state. For the $Se_{Cl}V_{Na}$ defect center, the ZFS parameter D, calculated using the expression $D = \frac{3}{2}D_{zz}$, yields a value of 7.94 GHz. This

TABLE III. The hyperfine tensors of the $Se_{Cl}V_{Na}$ defect calculated at the PBE level, and the atomic numbers in the table correspond to those depicted in Fig. 6(b).

Defects	Nuclear spins and natural abundance	Atoms	Hyperfine tensors (MHz) A_{xx}	A_{yy}	A_{zz}
$Se_{Cl}V_{Na}$	^{77}Se (I = 1/2, 7.63%)	Se	195.39	70.87	−453.05
	^{35}Cl (I = 3/2, 75.77%)	Cl_1, Cl_2	−5.86	0.36	24.28
	^{23}Na (I = 3/2, 100%)	Na_1, Na_2	0.88	0.61	3.74
		Na_3, Na_4	1.32	1.25	2.25
		Na_5, Na_6	−0.19	0.04	0.42
		Cl_3, Cl_4	−0.15	−0.09	0.91
		Cl_5, Cl_6	−0.19	0.11	−0.21

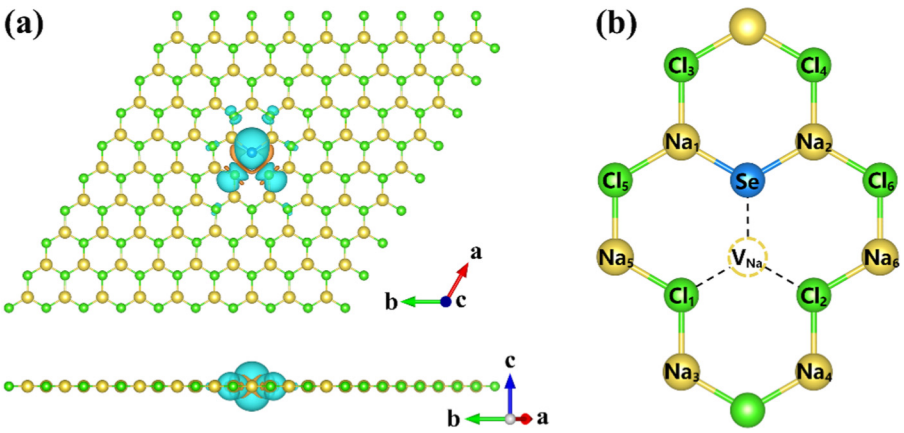

FIG. 6. Spin density of $Se_{Cl}V_{Na}$ (a) and schematic diagram of the defect center (b). Yellow and green spheres denote Na and Cl atoms, respectively. Cyan and orange denote positive and negative spin densities, respectively. The isosurface value is 5×10^{-5} e/Å^3.

represents a substantial enhancement compared to the 2.88 GHz ZFS value, characteristic of the NV^- center in diamond.[83] It is notable that this ZFS value falls within the microwave frequency range, facilitating high-temperature spin readout.[29] For a detailed overview of the diagonalization elements D_{xx}, D_{yy}, and D_{zz} of the ZFS tensor, refer to Table S5 in the supplementary material. It should be noted that the presence of heavy atom Se in the system could significantly change the final calculated value due to the SOC effect.[57]

On the other hand, hyperfine coupling represents the interaction between the electron spin and the nuclear spin, which can be defined as follows:

$$\hat{H}_{hyp} = \sum_{i,j} \hat{\vec{S}}_i A_{ij} \hat{\vec{I}}_j, \tag{9}$$

where $\hat{\vec{S}}$ and $\hat{\vec{I}}$ are the electron spin angular momentum operator and the nuclear spin angular momentum operator, respectively, that play crucial roles in the description of hyperfine interactions. The hyperfine tensor, A_{ij}, which characterizes these interactions, is composed of two primary components: the isotropic Fermi contact term and the anisotropic dipolar term. This hyperfine tensor is expressed as

$$A_{ij} = \frac{2}{3}\frac{\mu_0 \gamma_e \gamma_I \delta_{ij}}{S_z} \int \delta_T\left(\vec{r}\right) \rho_s\left(\vec{r} + \vec{R_I}\right) d\vec{r} + \frac{\mu_0}{4\pi}\frac{\gamma_e \gamma_I}{S_z} \int \frac{\rho_s\left(\vec{r} + \vec{R_I}\right)}{r^3} \frac{3r_i r_j - \delta_{ij} r^2}{r^2} d\vec{r}, \tag{10}$$

where γ_e and γ_I represent the electron and nuclear gyromagnetic ratio, respectively, of the nuclear at R_I. S_z denotes the expectation value of the z-component of the total electronic spin. ρ_s represents the spin density, and $\delta_T\left(\vec{r}\right)$ is a smearing function.[84] The hyperfine coupling results in spectral splitting in electron paramagnetic resonance (EPR), ODMR, and electron–nuclear double-resonance (ENDOR).[76]

Table III lists the hyperfine interaction tensors (A_{xx}, A_{yy}, and A_{zz}) for both the 12 nearest atoms surrounding the defect centers [Na_{1-6} and Cl_{1-6}, as illustrated in Fig. 6(b)] and the dopant atom. A distinct correlation is observed between the spatial proximity of atoms to the defect center and the magnitude of their hyperfine tensors: atoms in closer proximity to the $Se_{Cl}V_{Na}$ defect center exhibit significantly larger hyperfine tensors. This spatial dependence is further evidenced by the spin density distribution presented in Fig. 6(a), which demonstrates a pronounced localization of spin-polarized charge density at the defect center, with an exponential decay profile as a function of distance from the center. The values of these hyperfine tensors can be compared with the hyperfine structure measured in EPR spectra, allowing identification of the atom position at the defect center.[82]

IV. CONCLUSION

In summary, we have designed a monolayer graphene-like 2D NaCl with a wide bandgap of 6.31 eV and negligible SOC effect as a host material for spin qubits. The stability of 2D NaCl is supported by cohesive energy, AIMD results, and phonon spectrum analysis. The designed defect center $Se_{Cl}V_{Na}$ in 2D NaCl has spin triplet ground states, spin conservation in optical transitions, large ΔE_C and ΔE_V, and the excited state energy of the dark state is higher than that of its triplet bright state. However, the computed values of the ZPL, HR factor, and DW factor are 0.21 eV, 10.40, and 3.03×10^{-5}, respectively. These values indicate that if there are many effective phonons that participated in the optical transition, then non-radiative decay will be highly competitive with radiative decay during the transition. Notably, the zero-field splitting of the $Se_{Cl}V_{Na}$ defect falls within the microwave range, which is particularly suitable for quantum manipulation. Finally, the hyperfine tenors have been calculated to evaluate the interaction between the electron spin and the nuclear spin. In brief, we have performed systematic computational investigations to identify the potential qubit candidates in 2D NaCl. Although the current results do not reveal optimal qubit characteristics, this study provides fundamental insights into the design principles of solid-state spin qubits in 2D materials for quantum technology applications. Our work establishes an initial framework for exploring spin qubits in 2D NaCl,

and we anticipate that future theoretical and experimental investigations may identify promising qubit candidates within this material system.

SUPPLEMENTARY MATERIAL

See supplementary material for the total magnetic moment (μ_B) and partial orbital occupancy information of the considered defects; projected densities of states (PDOS) for various charged defect states; the total energies of triplet and singlet states of the $S_{Cl}V_{Na}$, $Se_{Cl}V_{Na}$, and $Te_{Cl}V_{Na}$ defects along with the energy difference; the structure of the optimized vacancy-doping defect pairs; electronic structures of the $S_{Cl}V_{Na}$, $Se_{Cl}V_{Na}$, and $Te_{Cl}V_{Na}$ defects; transition dipole moments of the $S_{Cl}V_{Na}$, $Se_{Cl}V_{Na}$, and $Te_{Cl}V_{Na}$ defects (unit in Debye); vertical absorption energy (E_a), vertical excitation energy (E_e), Stokes shift (ΔS), anti-Stokes shift (ΔAS), and zero-phonon line (ZPL) of the $Se_{Cl}V_{Na}$ defect; the zero-field splitting (ZFS) data of $Se_{Cl}V_{Na}$ after diagonalization (unit in MHz).

ACKNOWLEDGMENTS

The authors thank the National Natural Science Foundation of China (Grant No. 12164020) for financial support of the current work. Jijun Huang also thanks the Graduate Domestic and International Visiting Program of Jiangxi Normal University and the China Scholarship Council (Grant No. 202308360177). for partial support. We gratefully acknowledge the Hefei Advanced Computing Center for computational support.

AUTHOR DECLARATIONS

Conflict of Interest

The authors have no conflicts to disclose.

Author Contributions

Jijun Huang: Investigation (lead); Writing – original draft (lead). **Qiang Ke:** Conceptualization (equal); Data curation (equal). **Xueling Lei:** Funding acquisition (lead); Project administration (lead); Software (lead); Supervision (lead); Writing – review & editing (lead).

DATA AVAILABILITY

The data that support the findings of this study are available from the corresponding author upon reasonable request.

REFERENCES

[1]J. L. O'Brien, Science **318**, 1567 (2007).
[2]V. Scarani, H. Bechmann-Pasquinucci, N. J. Cerf, M. Dušek, N. Lütkenhaus, and M. Peev, Rev. Mod. Phys. **81**, 1301 (2009).
[3]H. K. Lo, M. Curty, and K. Tamaki, Nat. Photonics **8**, 595 (2014).
[4]C. L. Degen, F. Reinhard, and P. Cappellaro, Rev. Mod. Phys. **89**, 035002 (2017).
[5]D. Budker and M. Romalis, Nat. Phys. **3**, 227 (2007).
[6]A. Acín, I. Bloch, H. Buhrman, T. Calarco, C. Eichler, J. Eisert, D. Esteve, N. Gisin, S. J. Glaser, F. Jelezko, S. Kuhr, M. Lewenstein, M. F. Riedel, P. O. Schmidt, R. Thew, A. Wallraff, I. Walmsley, and F. K. Wilhelm, New J. Phys. **20**, 080201 (2018).
[7]M. De Michielis, E. Ferraro, E. Prati, L. Hutin, B. Bertrand, E. Charbon, D. J. Ibberson, and M. Fernando Gonzalez-Zalba, J. Phys. D: Appl. Phys. **56**, 363001 (2023).
[8]Y. Y. Jau, A. M. Hankin, T. Keating, I. H. Deutsch, and G. W. Biedermann, Nat. Phys. **12**, 71 (2016).
[9]J. Kelly, R. Barends, A. G. Fowler, A. Megrant, E. Jeffrey, T. C. White, D. Sank, J. Y. Mutus, B. Campbell, Y. Chen, Z. Chen, B. Chiaro, A. Dunsworth, I. C. Hoi, C. Neill, P. J. O'Malley, C. Quintana, P. Roushan, A. Vainsencher, J. Wenner, A. N. Cleland, and J. M. Martinis, Nature **519**, 66 (2015).
[10]A. Somoroff, Q. Ficheux, R. A. Mencia, H. Xiong, R. Kuzmin, and V. E. Manucharyan, Phys. Rev. Lett. **130**, 267001 (2023).
[11]C. Schimpf, F. B. Basset, M. Aigner, W. Attenender, L. Ginés, G. Undeutsch, M. Reindl, D. Huber, D. Gangloff, E. A. Chekhovich, C. Schneider, S. Höfling, A. Predojević, R. Trotta, and A. Rastelli, Phys. Rev. B **108**, L081405 (2023).
[12]B. C. Rose, D. Huang, Z. H. Zhang, P. Stevenson, A. M. Tyryshkin, S. Sangtawesin, S. Srinivasan, L. Loudin, M. L. Markham, A. M. Edmonds, D. J. Twitchen, S. A. Lyon, and N. P. de Leon, Science **361**, 60 (2018).
[13]F. F. Yan, A. L. Yi, J. F. Wang, Q. Li, P. Yu, J. X. Zhang, A. Gali, Y. Wang, J. S. Xu, X. Ou, C. F. Li, and G. C. Guo, npj Quantum Inf. **6**, 38 (2020).
[14]G. Wolfowicz, F. J. Heremans, C. P. Anderson, S. Kanai, H. Seo, A. Gali, G. Galli, and D. D. Awschalom, Nat. Rev. Mater. **6**, 906 (2021).
[15]G. Balasubramanian, P. Neumann, D. Twitchen, M. Markham, R. Kolesov, N. Mizuochi, J. Isoya, J. Achard, J. Beck, J. Tissler, V. Jacques, P. R. Hemmer, F. Jelezko, and J. Wrachtrup, Nat. Mater. **8**, 383 (2009).
[16]N. Bar-Gill, L. M. Pham, A. Jarmola, D. Budker, and R. L. Walsworth, Nat. Commun. **4**, 1743 (2013).
[17]R. Löfgren, R. Pawar, S. Öberg, and J. A. Larsson, New J. Phys. **21**, 053037 (2019).
[18]L. J. Rogers, K. D. Jahnke, M. W. Doherty, A. Dietrich, L. P. McGuinness, C. Müller, T. Teraji, H. Sumiya, J. Isoya, N. B. Manson, and F. Jelezko, Phys. Rev. B **89**, 235101 (2014).
[19]A. Dietrich, K. D. Jahnke, J. M. Binder, T. Teraji, J. Isoya, L. J. Rogers, and F. Jelezko, New J. Phys. **16**, 113019 (2014).
[20]A. Sipahigil, R. E. Evans, D. D. Sukachev, M. J. Burek, J. Borregaard, M. K. Bhaskar, C. T. Nguyen, J. L. Pacheco, H. A. Atikian, C. Meuwly, R. M. Camacho, F. Jelezko, E. Bielejec, H. Park, M. Lončar, and M. D. Lukin, Science **354**, 847 (2016).
[21]E. M. Y. Lee, A. Yu, J. J. de Pablo, and G. Galli, Nat. Commun. **12**, 6325 (2021).
[22]Q. Li, J. F. Wang, F. F. Yan, J. Y. Zhou, H. F. Wang, H. Liu, L. P. Guo, X. Zhou, A. Gali, Z. H. Liu, Z. Q. Wang, K. Sun, G. P. Guo, J. S. Tang, H. Li, L. X. You, J. S. Xu, C. F. Li, and G. C. Guo, Natl. Sci. Rev. **9**, nwab122 (2022).
[23]J. F. Wang, F. F. Yan, Q. Li, Z. H. Liu, H. Liu, G. P. Guo, L. P. Guo, X. Zhou, J. M. Cui, J. Wang, Z. Q. Zhou, X. Y. Xu, J. S. Xu, C. F. Li, and G. C. Guo, Phys. Rev. Lett. **124**, 223601 (2020).
[24]G. D. Bian, H. Yuan, N. Zhang, L. X. Xu, J. X. Zhang, P. C. Fan, H. L. Wang, C. Zhang, G. C. Shan, Q. F. Zhang, and J. C. Fang, Appl. Phys. Lett. **114**, 102105 (2019).
[25]A. J. Morfa, B. C. Gibson, M. Karg, T. J. Karle, A. D. Greentree, P. Mulvaney, and S. Tomljenovic-Hanic, Nano Lett. **12**, 949 (2012).
[26]Y. B. Chen, M. E. Turiansky, and C. G. Van de Walle, Phys. Rev. B **106**, 174113 (2022).
[27]C. Q. Zhou, Z. Y. Li, and J. L. Yang, Comput. Mater. Sci. **181**, 109754 (2020).
[28]X. P. Wang, M. W. Zhao, Z. H. Wang, X. J. He, Y. Xi, and S. S. Yan, Appl. Phys. Lett. **100**, 192401 (2012).
[29]Y. Lee, Y. Hu, X. Lang, D. Kim, K. Li, Y. Ping, K. C. Fu, and K. Cho, Nat. Commun. **13**, 7501 (2022).
[30]N. P. de Leon, K. M. Itoh, D. Kim, K. K. Mehta, T. E. Northup, H. Paik, B. S. Palmer, N. Samarth, S. Sangtawesin, and D. W. Steuerman, Science **372**, 253 (2021).
[31]B. Naydenov, F. Reinhard, A. Lämmle, V. Richter, R. Kalish, U. F. S. D'Haenens-Johansson, M. Newton, F. Jelezko, and J. Wrachtrup, Appl. Phys. Lett. **97**, 242511 (2010).

[32]Y. Chu, N. P. de Leon, B. J. Shields, B. Hausmann, R. Evans, E. Togan, M. J. Burek, M. Markham, A. Stacey, A. S. Zibrov, A. Yacoby, D. J. Twitchen, M. Loncar, H. Park, P. Maletinsky, and M. D. Lukin, Nano Lett. **14**, 1982 (2014).
[33]K. A. Cochrane, J. H. Lee, C. Kastl, J. B. Haber, T. Zhang, A. Kozhakhmetov, J. A. Robinson, M. Terrones, J. Repp, J. B. Neaton, A. Weber-Bargioni, and B. Schuler, Nat. Commun. **12**, 7287 (2021).
[34]E. Glushkov, M. Macha, E. Räth, V. Navikas, N. Ronceray, C. Y. Cheon, A. Ahmed, A. Avsar, K. Watanabe, T. Taniguchi, I. Shorubalko, A. Kis, G. Fantner, and A. Radenovic, ACS Nano **16**, 3695 (2022).
[35]Y. Ping and T. J. Smart, Nat. Comput. Sci. **1**, 646 (2021).
[36]S. Ali, F. A. Nilsson, S. Manti, F. Bertoldo, J. J. Mortensen, and K. S. Thygesen, ACS Nano **17**, 21105 (2023).
[37]G. Cassabois, P. Valvin, and B. Gil, Nat. Photonics **10**, 262 (2016).
[38]W. Liu, N.-J. Guo, S. Yu, Y. Meng, Z.-P. Li, Y.-Z. Yang, Z.-A. Wang, X.-D. Zeng, L.-K. Xie, Q. Li, J.-F. Wang, J.-S. Xu, Y.-T. Wang, J.-S. Tang, C.-F. Li, and G.-C. Guo, Mater. Quantum Technol. **2**, 032002 (2022).
[39]T. T. Tran, K. Bray, M. J. Ford, M. Toth, and I. Aharonovich, Nat. Nanotechnol. **11**, 37 (2016).
[40]P. Auburger and A. Gali, Phys. Rev. B **104**, 075410 (2021).
[41]Z. Benedek, R. Babar, Á Ganyecz, T. Szilvási, Ö Legeza, G. Barcza, and V. Ivády, npj Comput. Mater. **9**, 187 (2023).
[42]A. Gottscholl, M. Diez, V. Soltamov, C. Kasper, A. Sperlich, M. Kianinia, C. Bradac, I. Aharonovich, and V. Dyakonov, Sci. Adv. **7**, eabf3630 (2021).
[43]S. Vaidya, X. Y. Gao, S. Dikshit, I. Aharonovich, and T. C. Li, Adv. Phys.: X **8**, 2206049 (2023).
[44]A. Sajid, J. R. Reimers, R. Kobayashi, and M. J. Ford, Phys. Rev. B **102**, 144104 (2020).
[45]S. Li and A. Gali, J. Phys. Chem. Lett. **13**, 9544 (2022).
[46]A. Sajid, K. S. Thygesen, J. R. Reimers, and M. J. Ford, Commun. Phys. **3**, 153 (2020).
[47]F. Wu, A. Galatas, R. Sundararaman, D. Rocca, and Y. Ping, Phys. Rev. Mater. **1**, 071001 (2017).
[48]G. D. Cheng, Y. G. Zhang, L. Yan, H. F. Huang, Q. Huang, Y. X. Song, Y. Chen, and Z. Tang, Comput. Mater. Sci. **129**, 247 (2017).
[49]P. Udvarhelyi, T. Clua-Provost, A. Durand, J. H. Li, J. H. Edgar, B. Gil, G. Cassabois, V. Jacques, and A. Gali, npj Comput. Mater. **9**, 150 (2023).
[50]A. Gottscholl, M. Kianinia, V. Soltamov, S. Orlinskii, G. Mamin, C. Bradac, C. Kasper, K. Krambrock, A. Sperlich, M. Toth, I. Aharonovich, and V. Dyakonov, Nat. Mater. **19**, 540 (2020).
[51]A. Gottscholl, M. Diez, V. Soltamov, C. Kasper, D. Krauße, A. Sperlich, M. Kianinia, C. Bradac, I. Aharonovich, and V. Dyakonov, Nat. Commun. **12**, 4480 (2021).
[52]W. Liu, Z. P. Li, Y. Z. Yang, S. Yu, Y. Meng, Z. A. Wang, Z. C. Li, N. J. Guo, F. F. Yan, Q. Li, J. F. Wang, J. S. Xu, Y. T. Wang, J. S. Tang, C. F. Li, and G. C. Guo, Acs Photonics **8**, 1889 (2021).
[53]X. Lyu, Q. Tan, L. Wu, C. Zhang, Z. Zhang, Z. Mu, J. Zúñiga-Pérez, H. Cai, and W. Gao, Nano Lett. **22**, 6553 (2022).
[54]J. Lee, H. Park, and H. Seo, npj 2D Mater. Appl. **6**, 60 (2022).
[55]R. Rizzato, M. Schalk, S. Mohr, J. C. Hermann, J. P. Leibold, F. Bruckmaier, G. Salvitti, C. Qian, P. Ji, G. V. Astakhov, U. Kentsch, M. Helm, A. V. Stier, J. J. Finley, and D. B. Bucher, Nat. Commun. **14**, 5089 (2023).
[56]A. Srivastava, M. Sidler, A. V. Allain, D. S. Lembke, A. Kis, and A. Imamoğlu, Nat. Nanotechnol. **10**, 491 (2015).
[57]S. Li, G. Thiering, P. Udvarhelyi, V. Ivády, and A. Gali, Nat. Commun. **13**, 1210 (2022).
[58]K. Barthelmi, J. Klein, A. Hötger, L. Sigl, F. Sigger, E. Mitterreiter, S. Rey, S. Gyger, M. Lorke, M. Florian, F. Jahnke, T. Taniguchi, K. Watanabe, V. Zwiller, K. D. Jöns, U. Wurstbauer, C. Kastl, A. Weber-Bargioni, J. J. Finley, K. Müller, and A. W. Holleitner, Appl. Phys. Lett. **117**, 070501 (2020).
[59]C. J. H. Wort and R. S. Balmer, Mater. Today **11**, 22 (2008).
[60]B. Luo, Y. Yao, E. Tian, H. Song, X. Wang, G. Li, K. Xi, B. Li, H. Song, and L. Li, Proc. Natl. Acad. Sci. U.S.A. **116**, 17213 (2019).
[61]B. N. Nguyen Thi, C. V. Ha, N. Thi Ha Lien , J. Guerrero-Sanchez, and D. M. Hoat, Phys. Chem. Chem. Phys. **25**, 32569 (2023).
[62]K. A. Tikhomirova, C. Tantardini, E. V. Sukhanova, Z. I. Popov, S. A. Evlashin, M. A. Tarkhov, V. L. Zhdanov, A. A. Dudin, A. R. Oganov, D. G. Kvashnin, and A. G. Kvashnin, J. Phys. Chem. Lett. **11**, 3821 (2020).
[63]G. Kresse and J. Hafner, Phys. Rev. B **47**, 558 (1993).
[64]G. Kresse and J. Furthmüller, Phys. Rev. B **54**, 11169 (1996).
[65]G. Kresse and D. Joubert, Phys. Rev. B **59**, 1758 (1999).
[66]P. E. Blöchl, Phys. Rev. B **50**, 17953 (1994).
[67]J. P. Perdew, K. Burke, and M. Ernzerhof, Phys. Rev. Lett. **77**, 3865 (1996).
[68]H. J. Monkhorst and J. D. Pack, Phys. Rev. B **13**, 5188 (1976).
[69]J. Heyd, G. E. Scuseria, and M. Ernzerhof, J. Chem. Phys. **118**, 8207 (2003).
[70]P. Deák, B. Aradi, T. Frauenheim, E. Janzén, and A. Gali, Phys. Rev. B **81**, 153203 (2010).
[71]A. Togo and I. Tanaka, Scr. Mater. **108**, 1 (2015).
[72]A. Gali, E. Janzén, P. Deák, G. Kresse, and E. Kaxiras, Phys. Rev. Lett. **103**, 186404 (2009).
[73]J. R. Weber, W. F. Koehl, J. B. Varley, A. Janotti, B. B. Buckley, C. G. Van de Walle, and D. D. Awschalom, Proc. Natl. Acad. Sci. U.S.A. **107**, 8513 (2010).
[74]M. Kan, S. Adhikari, and Q. Sun, Phys. Chem. Chem. Phys. **16**, 4990 (2014).
[75]J. S. Zhang, Y. Wang, C. Q. Hua, S. B. Yang, Y. J. Liu, J. M. Luo, T. F. Liu, J. Nai, and X. Y. Tao, Phys. Rev. B **106**, 235401 (2022).
[76]C. E. Dreyer, A. Alkauskas, J. L. Lyons, A. Janotti, and C. G. Van de Walle, Annu. Rev. Mater. Res. **48**, 1 (2018).
[77]H.-P. Komsa, T. T. Rantala, and A. Pasquarello, Phys. Rev. B **86**, 045112 (2012).
[78]C. Freysoldt, J. Neugebauer, and C. G. Van de Walle, Phys. Rev. Lett. **102**, 016402 (2009).
[79]M. H. Naik and M. Jain, Comput. Phys. Commun. **226**, 114 (2018).
[80]C. Freysoldt, B. Grabowski, T. Hickel, J. Neugebauer, G. Kresse, A. Janotti, and C. G. Van de Walle, Rev. Mod. Phys. **86**, 253 (2014).
[81]C. Qian, V. Villafañe, M. Schalk, G. V. Astakhov, U. Kentsch, M. Helm, P. Soubelet, N. P. Wilson, R. Rizzato, S. Mohr, A. W. Holleitner, D. B. Bucher, A. V. Stier, and J. J. Finley, Nano Lett. **22**, 5137 (2022).
[82]M. Mohseni, I. A. Sarsari, S. Karbasizadeh, P. Udvarhelyi, Q. Hassanzada, T. Ala-Nissila, and A. Gali, Phys. Rev. Mater. **8**, 056201 (2024).
[83]V. Ivády, T. Simon, J. R. Maze, I. A. Abrikosov, and A. Gali, Phys. Rev. B **90**, 235205 (2014).
[84]P. E. Blöchl, Phys. Rev. B **62**, 6158 (2000).